frontiers in Energy Research

ORIGINAL RESEARCH
published: 29 November 2021
doi: 10.3389/fenrg.2021.794527

Facile Construction of Hierarchical $TiNb_2O_7$/rGO Nanoflower With Robust Charge Storage Properties for Li Ion Batteries via an Esterification Reaction

Lei Hu[1,2], Xulai Yang[3], Yumeng Chen[1], Lili Wang[1,2], Jiajia Li[2], Yujie Tang[2] and Haitao Zhang[1,2]**

[1]School of Energy Materials and Chemical Engineering, Hefei University, Hefei, China, [2]Beijing Key Laboratory of Ionic Liquids Clean Process, CAS Key Laboratory of Green Process and Engineering, Institute of Process Engineering, Chinese Academy of Sciences, Beijing, China, [3]School of Advanced Manufacturing Engineering, Hefei University, Hefei, China

OPEN ACCESS

Edited by:
Chao Han,
University of Technology Sydney, Australia

Reviewed by:
Qingbing Xia,
The University of Queensland, Australia
Zhijia Zhang,
Tiangong University, China

***Correspondence:**
Xulai Yang
yangxl@hfuu.edu.cn
Haitao Zhang
htzhang@ipe.ac.cn

Specialty section:
This article was submitted to Electrochemical Energy Conversion and Storage, a section of the journal Frontiers in Energy Research

Received: *13 October 2021*
Accepted: *28 October 2021*
Published: *29 November 2021*

Citation:
Hu L, Yang X, Chen Y, Wang L, Li J, Tang Y and Zhang H (2021) Facile Construction of Hierarchical $TiNb_2O_7$/rGO Nanoflower With Robust Charge Storage Properties for Li Ion Batteries via an Esterification Reaction. Front. Energy Res. 9:794527. doi: 10.3389/fenrg.2021.794527

$TiNb_2O_7$ (TNO) compound has been pursued tremendously due to its high theoretical capacity, high potential, and excellent cycle stability. Unfortunately, an intrinsic low electronic and ionic conductivity feature has restricted its broad applications in electrochemical energy storage fields. Two-dimensional (2D) nanostructures can effectively shorten Li-ion transport path and enhance charge transfer. Here, hierarchical structure TNO was constructed by using ethanol and acetic acid as particularly important organic chemicals of basic raw materials via a simple solvothermal reaction. Ethanol was found to play a critical role in the formation of 2D sheet structure. Meantime, reduced graphene oxide nanosheets can effectively improve electronic conductivity. As-obtained $TiNb_2O_7$ were wrapped further by graphene oxide nanosheets through a flocculation process. Their unique structure is beneficial to the final electrochemical performance. This study not only provides a general approach for the design of novel 2D nanomaterials wrapped by graphene because of the advantage of esterification reaction and flocculation reaction, but also improves the electronic and ionic conductivity simultaneously.

Keywords: $TiNb_2O_7$, esterification reaction, two-dimensional sheet, graphene, li ion batteries

INTRODUCTION

Lithium ion batteries (LIBs) have shown great potential in portable devices and electric vehicles owing to their high energy and power densities (Yang et al., 2020; Baek et al., 2021; Hu et al., 2021; Liu et al., 2021a; Zhang et al., 2021a; Zhang et al., 2021b; Guo et al., 2021; He et al., 2021). However, with the rise in demand in the consumer market, LIBs require further higher power density, profound safety, and long-life. Though graphite is used as an ideal anode material in commercial LIBs, its lower electrochemical potential can cause serious safety issues. Besides, lower capacity and easy formation of solid electrolyte interface (SEI) film consumption of electrolyte are also disadvantages of graphite electrode materials. $TiNb_2O_7$ has been extensively investigated as a promising anode material because of its merits in the field of Li-ion batteries, such as high theoretical capacity (388 mA h g^{-1}), high discharge voltage (1.65 V), and long life span (Han et al., 2011; Tang et al., 2013; Guo et al., 2014). $TiNb_2O_7$ (TNO) has the space group C2/m, which lithium atoms have been stored in the (110)

plane with four different coordinations positions (Lu et al., 2011). Unfortunately, the electrochemical performance of $TiNb_2O_7$ materials is severely constrained by low ion diffusion diffusivity (10^{17} cm (Baek et al., 2021) s^{-1}) (Gao et al., 2017) and poor conductivity ($<1.0 \times 10^{-9}$ S cm^{-1}) (Lin et al., 2015).

Therefore, a series of work mainly focuses on the modification of two aspects. Carbon coating is considered to be an effective way to address poor conductivity to enhance the electrochemical performance. In previous literature, the research on carbon source for carbon coating mainly comes from heteroatom-doped carbon (Yang et al., 2021a; Yang et al., 2021b), biomass carbon (Thiyagarajan et al., 2021), CNT (Lin et al., 2018; Zhu et al., 2022), and graphene (Ashish et al., 2015; Li et al., 2016; Liu et al., 2021b). For instance, Shaijumona et al. (Ashish et al., 2015) obtained $TiNb_2O_7$/graphene composited by simple solvothermal process, which realized TNO nanoparticles anchored on the reduced graphene oxide. Lately, Cao et al. (Li et al., 2016) prepared nano-sized TNO materials with graphene oxide by ultrasonic dispersion and annealing treatment under inert atmosphere. However, the TNO products obtained from the above studies are limited to graphene warped nano-level TNO, while micron-sized TNO is easily affected by sedimentation in graphene oxide solution. Therefore, it is difficult to achieve homogeneous TNO/graphene composite due to the lack of sufficient electrostatic driving force and contact area. Achieving a close contact structure of TNO/graphene composite under simple conditions will have greater significance in improving electronic conductivity.

In order to ameliorate low ionic conductivity, many researchers have been focusing on shortening lithium diffusion length, such as reducing the particle sizes and constructing different structures. Thus far, various nanostructures, such as hollow sphere (Zhu et al., 2018), rods (Lou et al., 2015), fiber (Park et al., 2015), and nano-pearl-string-like (Tang et al., 2013), have been developed to enhance ionic conductivity, which presents admirable improvements. For instance, 2D nanomaterials can effectively reduce the length of lithium ions transportation paths to improve its diffusion rate and its electrochemical performance (Yin et al., 2020). Recently, three-dimensional porous $TiNb_2O_7$/CNT-KB composite was fabricated by spray drying and solvothermal method. Benefiting from three-dimensional porous structure, the electrodes were maintained about 45.7% capacity retention (81.9 mA h g^{-1}) at the current rate of 5°C after 1000 cycles (Liu et al., 2019). Among these nanostructures, sphere morphology with low interface energy, high tap density, and uniform electrochemical stability has been attracting a lot of attention in industrial applications. The micro-sized sphere TNO can be easily fabricated by traditional solvothermal synthesis routes using various surfactant or block copolymers, such as P123 (Yang et al., 2016) and F127 (Guo et al., 2014). However, these methods are inevitably accompanied by a template-removal process that might cause degradation of performances. Besides, the fabrication of TNO is often based on the hydrolysis reaction of niobium and titanium salts (Ding et al., 2011). Therefore, to prepare TNO with various nanostructures, the better way is to reasonably control the hydrolysis reaction without any surfactants. Although traditional solvothermal synthesis routes have already shown incomparable advantages in reducing the particle size and homogeneity, exploring an effective way to control the growth of orientation is still extensively desired.

Currently, more studies are mainly focused on two or more strategies, which demonstrates the synergistic effect of various modification strategies is an effective way to promote the shortcomings of TNO (ion diffusion diffusivity and electronic conductivity). For example, Zhang et al. (Liu et al., 2021b) reported that $TiNb_2O_7$ nanoparticles anchored on bended graphene nanosheets presents superior electrochemical performance benefit from shortening the length of ion transport and increasing the electrical conductivity. In this work, we successfully fabricated hierarchical $TiNb_2O_7$ by controlling the degree of hydrolysis of esterification reaction. The layered structure of TNO provides efficient Li^+ ion migration and superior rate capability. Previous study indicates that the controlled formation of the flower-like structure can be achieved by varying water produced during the esterification reactions between acid and alcohol (Fu et al., 2014). The growth of the hierarchical nanoflower structure can be divided into several separative steps as follows. First, the alcoholysis of $NbCl_5$ occurs due to the presence of ethanol (Kumar and Sahay, 2019). Previous reports (Fu et al., 2014; Kumar and Sahay, 2019) suggest that the addition of alcoholysis of $NbCl_5$ can modulate the surrounding chemical environment, and the introduction of acetic acid as a hydrolysis and condensing agent can lead to the formation of complex via a reaction with alkoxide, make the alkoxide to be nucleated more uniformly, and effectively hinder the hydrolysis, and thereby prevent unexpected precipitation. Based on these reactions, we have achieved the control of oriented growth of TNO materials. Furthermore, we introduced polyacrylamide (PAM) as a binder that provides the attachment mechanism between GO and TNO. As we all known, polyacrylamide has been extensively used as flocculant in water treatment for removing micro-sized pollutant (Kankanige and Babel, 2021). Hence, PAM has a high adhesion ability to the TNO surface, and hierarchical TNO are densely adhered to the GO surface via a simple mixing process. Finally, a compact TNO/rGO composite is formed after annealing treatment, which realizes the graphene wrapped micron-level TNO. This effective carbon coating of TNO provides a conductive network of electrons, which can greatly improve robust charge storage and rapid charge-discharge capability.

$$NbCl_5 + 5CH_3CH_2OH \rightarrow Nb(OCH_2CH_3)_5 + 5HCl \quad (1)$$

$$Ti(OC_4H_9)_4 + xCH_3COOH \rightarrow Ti(CH_3COO)_x(OC_4H_9)_{4-x} + xC_4H_9OH \quad (2)$$

$$Nb(OCH_2CH_3)_5 + yCH_3COOH \rightarrow Nb(CH_3COO)_y(OCH_2CH_3)_{5-y} + yCH_3CH_2OH \quad (3)$$

$$C_4H_9OH + CH_3COOH \xrightarrow{Esterification} CH_3COOC_4H_9 + H_2O \quad (4)$$

$$CH_3CH_2OH + CH_3COOH \xrightarrow{Esterification} CH_3COOCH_2CH_3 + H_2O \quad (5)$$

$$\begin{pmatrix} Ti(CH_3COO)_x(OC_4H_9)_{4-y} \\ Nb(CH_3COO)_y(OCH_2CH_3)_{5-y} \end{pmatrix} + H_2O \xrightarrow{Hydrolysis}$$

$$TiNb_2O_7 \begin{pmatrix} (x+y)CH_3COOH \\ (4-x)C_4H_9OH \\ (5-y)CH_3CH_2OH \end{pmatrix} \quad (6)$$

EXPERIMENTAL SECTION

Reagents

Niobium chloride ($NbCl_5$), titanium (IV) butoxide ($Ti(OC_4H_9)_4$, acetic acid (≥99.5%), and ethyl alcohol (≥99.7%) were purchased from Aladdin-Reagent Co., Ltd. All reagents are of analytical grade and were used without further purification.

Synthesis of Pristine TNO

Pristine TNO was prepared through a solvothermal reaction. Typically, a homogeneous transparent solution was prepared by mixing with 5.4 g of niobium chloride ($NbCl_5$) and 0.34 ml of titanium (IV) butoxide ($Ti(OC_4H_9)_4$), which was added into a solution containing 9 ml of ethanol and 2 ml of acetic acid. Then, the solution was transferred to a Teflon-lined stainless-steel autoclave (80 ml capacity) and kept in an oven at 200°C for 24 h. The obtained yellowish precipitate was centrifuged and washed with ethanol several times. The powder was dried in an oven at 80°C overnight and then calcined at 750°C in air for 3 h (a heating rate of 5°C min^{-1}) in a tube furnace to obtain pristine TNO.

Synthesis of Aqueous Dispersed Graphene Oxide

GO powder was made according to a slightly modified Hummer's method (Hummers and Offeman, 1958). Collected precipitate (0.5 g) was dispersed in water (500 ml) and ultra-sonicated for 1 h. After 4000 rpm centrifuge for 10 min, a yellow homogeneous supernatant of GO (1 mg ml^{-1}) was obtained.

Fabrication of TNO/NC and TNO/NC/GO Composite

A total of 80 mg of pristine TNO was dispersed into deionized water under ultrasonic treatment for 20 min. Then, 2 ml of PAM solution (1wt%) was added drop by drop into the above suspension to initiate the cross-linking reaction with magnetic stirring, until a flocculation appeared and the solution became clear and transparent. Finally, the product was collected and annealled at 750°C in Ar atmosphere for 3 h, leading to formation of TNO/NC nanocompoiste. As to the synthesis of TNO/NC/GO composite, the fabrication process is identical to that of TNO/NC, except that the powder is dispersed in graphene instead of deionized water.

Material Characterization

The morphology and structure of these samples were characterized by X-ray diffraction [Philips X'Pert Super diffractometer with Cu Kα radiation (λ = 1.54178 Å)], Raman spectrometer (Lab-RAM HR UV/vis/NIR), scanning electron microscopy (SEM) (Hitachi SU8060), and transmission electron microscopy (TEM) (JEOL-2010). Energy-dispersive spectrometry (EDS) elemental mapping was detected using an Oxford Instruments EDS system.

Electrochemical Measurements

To prepare the working electrode, a mixed slurry of active material, super P carbon black, and polyvinylidene fluoride (PVDF) with a mass ratio of 70:25:5 was coated onto Cu foil (99.9%). After being dried at 100°C for 10 h in a vacuum oven, the active material density of each electrode was determined to be around 1.0–1.5 mg cm^{-2}. The cells were assembled in an argon-filled glove box (H_2O, O_2 < 1 ppm). Celgard-2400 (Celgard) acted as a separator, and lithium foil was employed to a reference electrode. The electrolyte was 1 M $LiPF_6$ in ethylene carbonate and diethyl carbonate (1:1, a volume ratio). The $LiFePO_4$// $TiNb_2O_7$ full cell were also assembled into a coin cell with $TiNb_2O_7$ as the anodes and $LiFePO_4$ as the cathodes in the same electrolyte. The typical weight ratio of the negative/positive electrode employed is 1:1.4. The electrode was punched into circular disks (12 mm in diameter). The areal loading of the anode and cathode is 1 mg cm^{-2} and 1.4 mg cm^{-2}, respectively. Galvanostatic charge/discharge measurements were performed on a LAND-CT2001A instrument in the voltage range of 1–3 V (vs. Li/Li^+). Electrochemical impedance spectroscopy (EIS) was also measured with an electrochemical workstation (CHI660D) by applying an alternating current (AC) voltage of 5 mV in the frequency range from 100 kHz to 0.1 Hz. The structure evolution of TNO material was investigated by *in situ* X-ray diffraction (XRD) on the Rigaku Smart Lab at a current density of 1 C in the 2θ range from 20 to 50° with a scanning rate of 5°min^{-1}.

RESULTS AND DISCUSSION

For the fabrication of the TNO/NC/GO composite, three major procedures are involved (**Figure 1**). The first step is the solvothermal synthesis of TNO hierarchical nanoflower structure, where niobium chloride ($NbCl_5$) and tetrabutyl titanate ($C_{16}H_{36}O_4Ti$) were utilized as the niobium and titanium precursors, respectively (detailed experimental procedures are described in the Experimental section). As shown in **Figure 1**, the second step is the simple cross-linked reaction of TNO/NC/GO. For this step, a graphene oxide (GO) and TNO particles are well-dispersed in an aqueous solution to form a homogeneous suspension and subsequently added 1% PAM gel solution. The addition of flocculant promotes agglomeration between graphene oxide (GO) and TNO particles due to the positive and negative charge interaction (Kankanige and Babel, 2021), which would enhance effective surface contact and density of

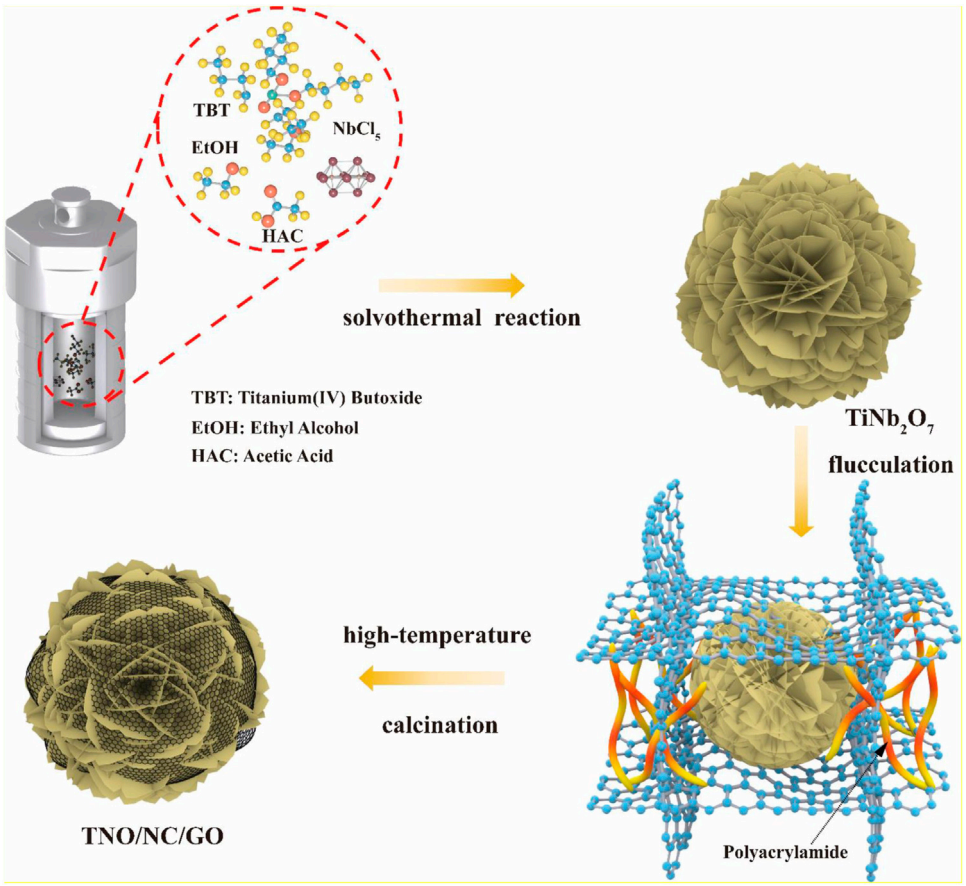

FIGURE 1 | Schematic process of the formation of TNO/NC/GO composite.

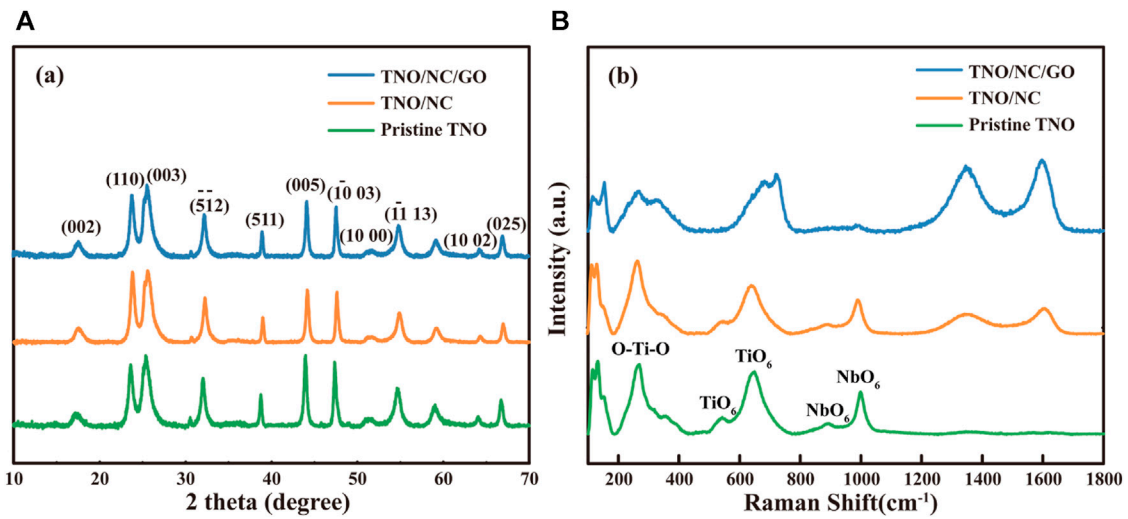

FIGURE 2 | (A) XRD patterns of pristine TNO, TNO/NC, and TNO/NC/GO nanocomposites; **(B)** Raman spectra of pristine TNO, TNO/NC, and TNO/NC/rGO nanostructures.

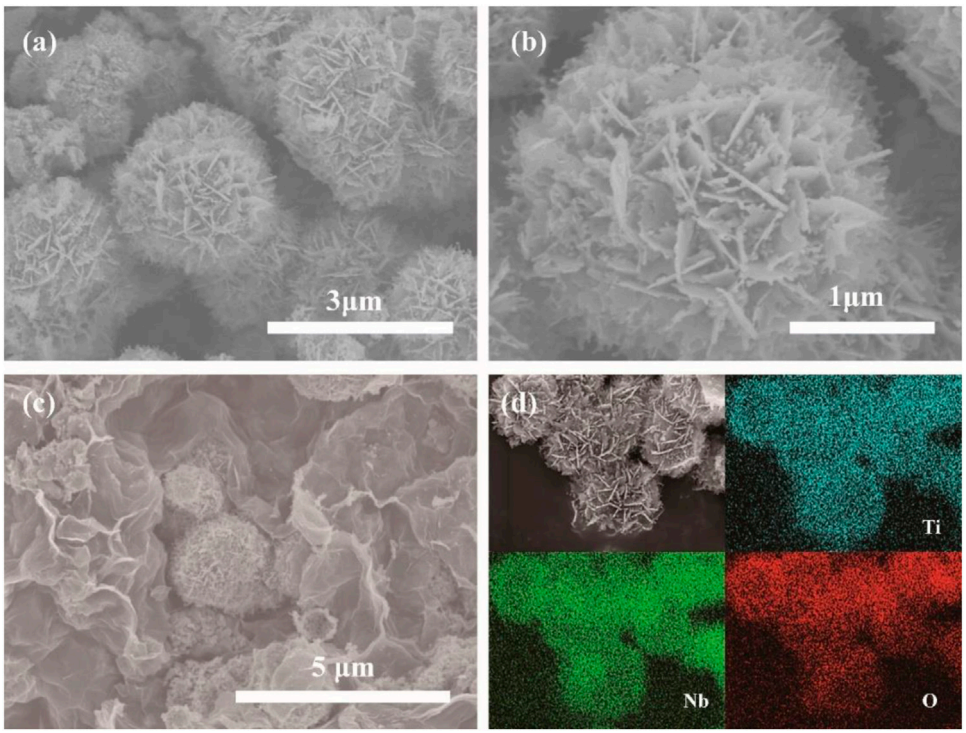

FIGURE 3 | (A) SEM image of pristine TNO, **(B)** enlarged magnification SEM image of pristine TNO, **(C)** SEM image of TNO/NC/GO, **(D)** EDS mapping of different elements.

encapsulation. As shown in **Supplementary Figure S1**, the color of well-dispersed mixed solution of GO and TNO gradually became colorless, due to the formation of precipitate by flocculation. The third step is high-temperature calcination, which obtained a tightly wrapped porous product TNO/NC/GO composite with the removal of the solvent and reduction of graphene oxide. After this treatment, TNO hierarchical nanoflower structure wrapped into graphene oxide consequently conquers the agglomeration issue and increases the available surface area resulting in high electrochemical activity.

Figure 2A depicts the X-ray diffraction (XRD) patterns of TNO, TNO/NC, and TNO/NC/GO. All appeared XRD peaks of TNO/NC/GO can be identified to that of pristine monoclinic $TiNb_2O_7$ sample (JCPDS card no. 77–1,374). No obvious peaks related to mono-oxides (such as TiO_2 or Nb_2O_5) are detected, indicating the formation of pure $TiNb_2O_7$. Moreover, the diffraction peak of GO was not observed in the TNO/NC/GO, implying that the GO has been reduced well through the annealing process and turned into graphene.

To further investigate to confirm the evidence of TNO and rGO, Raman spectroscopy of samples is presented in **Figure 2B**, the bands at 1005 and 882 cm^{-1} are three typical vibrations of the NbO_6. While the peaks at 650, 532 cm^{-1} demonstrates the vibration of TiO_6 octahedral (Lou et al., 2017). Moreover, the Raman shifts of TNO/NC/GO display two obvious peaks (D, G) at 1346 and 1580 cm^{-1}, which are reprehensive characteristics of amorphous carbon (Park et al., 2017). The ratio value between D/G bands (I_D/I_G) was 0.89, indicating the existence disordered amorphous carbon in ordered graphene, which would enhance the ion conductivity of rGO-wrapped TNO. To confirm the content of carbon coating, TGA curves were shown in **Supplementary Figure S2A**. The TNO/NC/GO powders have a significant weight loss at 520°C, corresponding to removal of the carbon (Chen et al., 2015), demonstrating that the content of carbon coating is 9.6%. Meantime, the carbon content of TNO/NC is 2.1% (**Supplementary Figure S2B**). The carbon content of GO contribution is 7.7% by calculating as in the Supporting Information.

Scanning electron microscopy (SEM) characterization was carried out to investigate the microstructure and morphology of as-synthesized samples. **Figure 3A** exhibits an overall SEM image of pristine TNO particles obtained after calcination under an Ar atmosphere at 750°C for 3 h. The uniform distribution of TNO hierarchical nanoflower structure is beneficial to prevent the TNO microstructure from agglomerating, and forms a better dispersion of TNO hierarchical nanoflower structure on graphene which promotes low capacity loss during cycling. **Figure 3B** displays an image of a small visual field, and shows the overall structure of the hierarchical nano-architectures of the pristine TNO. From **Figure 3B**, it can be clearly seen that pristine TNO has a homogeneous hierarchical nanoflower structure which consists of layer nanosheets with thickness of 30–50 nm. **Figure 3C** presents graphene layers as a spacer surrounding around the TNO microsphere. Moreover, the growth and aggregation of the TNO particles might be

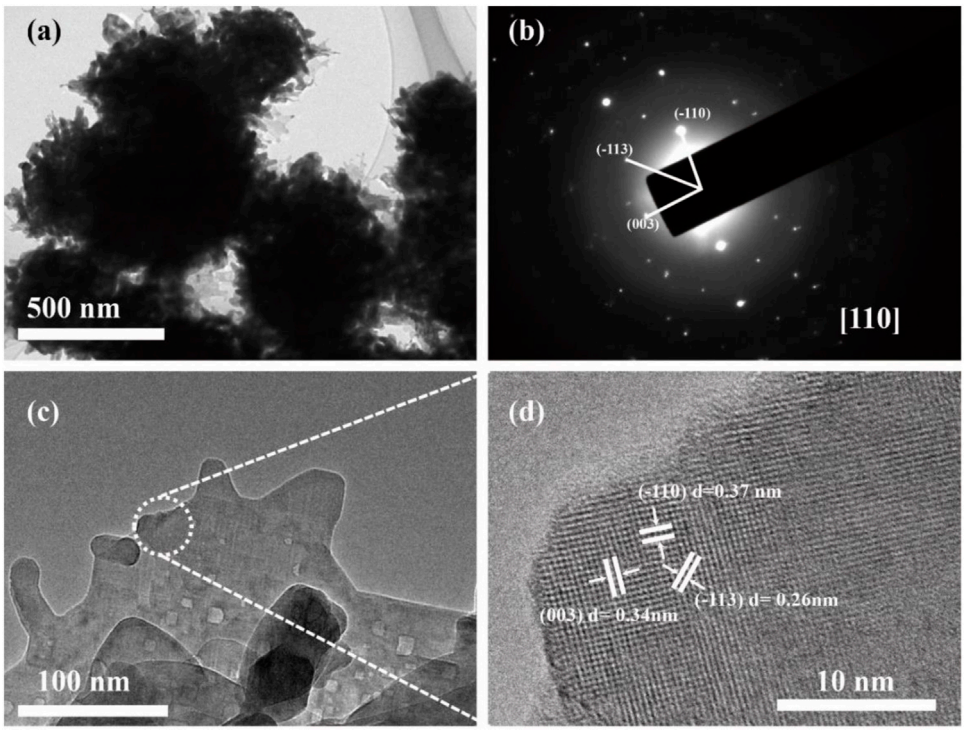

FIGURE 4 | (A) TEM image of pristine TNO; **(B)** SAED pattern of pristine TNO; **(C)** enlarged magnification TEM image of pristine TNO; **(D)** HRTEM image of pristine TNO.

conspicuously suppressed by graphene sheets. Besides, the energy dispersive X-ray mappings of pristine TNO also validate the presence of titanium, niobium, and oxygen elements, which are distributed homogeneously in the composite shown in **Figure 3D**.

Figure 4A shows the typical TEM images of pristine TNO with sphere structure around 500 nm in diameter. More detailed morphology structure can be found from the HRTEM image in **Figure 4C**, where a layered secondary structure can be clearly observed, suggesting the presence of a well-defined crystal structure. The periodic lattice fringe spacing of 0.37 nm is associated with interplanar spacing of (−110) planes of monoclinic $TiNb_2O_7$ which further corroborate the findings from the XRD results. As shown in **Figure 4D**, the atomic lattices can be clearly resolved, the lattice fringe spacing of 3.7, 3.4, and 2.6Å marked on their surfaces can be indexed to the (−110), (003), and (−113) reflections of $TiNb_2O_7$. The obtained from selected areas of the corresponding single crystal indicated that they were single crystals sitting against a plane perpendicular to the <110> zone axis, confirming that the (110) facets were exposed on the surface.

To confirm the electrochemical activity of the rGO wrapping on the TNO, CV experiments were initially performed. The first curves of pristine TNO, TNO/NC, and TNO/NC/GO were carried out at a scan rate of 0.1 mV s^{-1} in the potential range of 1.0–3.0 V (vs. Li/Li^+), as shown in **Figure 5A**. Compared with pristine TNO and TNO/NC, TNO/NC/GO displayed larger response currents, indicating a higher electrochemical activity due to enhancement of conduction (Han et al., 2014). At the same time, the current response of the TNO/NC is between pristine TNO and TNO/NC/GO composite, implying that NC has a positive effect on improving electrochemical performance. The voltammogram of TNO/NC/GO depicted one pair of sharp cathodic/anodic peaks at 1.55/1.72 V, attributing to the redox couple of Nb^{5+}/Nb^{4+}, while the peaks at around 1.80/1.92 V for TNO/NC/GO, can be assigned to the Ti^{4+}/Ti^{3+} couple, and the broad bump in the range of 1.0–1.4 V may be assigned to the Nb^{4+}/Nb^{3+} redox couple (Lin et al., 2018). The symmetrical feature of the CV curves suggests a good reversibility of the cycling process (**Figure 5B**). As shown in **Supplementary Figure S3A–C**, the intensity of these peaks increases with the increase of scan rate from 0.1 mV s^{-1} to 1 mV s^{-1}, however, the position of TNO/NC/GO exhibits minimal variation, indicating the fast charge transfer in the process.

Moreover, to further investigate the difference of pseudocapacitive behavior among pristine TNO, TNO/NC, and TNO/NC/GO.

According to the corresponding power-law relation:

$$i = av^b \tag{7}$$

where i represents the current response, ν denotes the scanning rate, and a and b are constants. **Figure 5C** shows the plot of log(i) vs. log (ν), where the slope of the linear line corresponds to the b-value. While the b = 0.5 indicates an ideal diffusion-controlled process, while that of the b = 1 indicates a surface capacitive-controlled one. The b-value was calculated to be 0.84 for TNO/NC/GO composites, indicating that the capacity was contributed

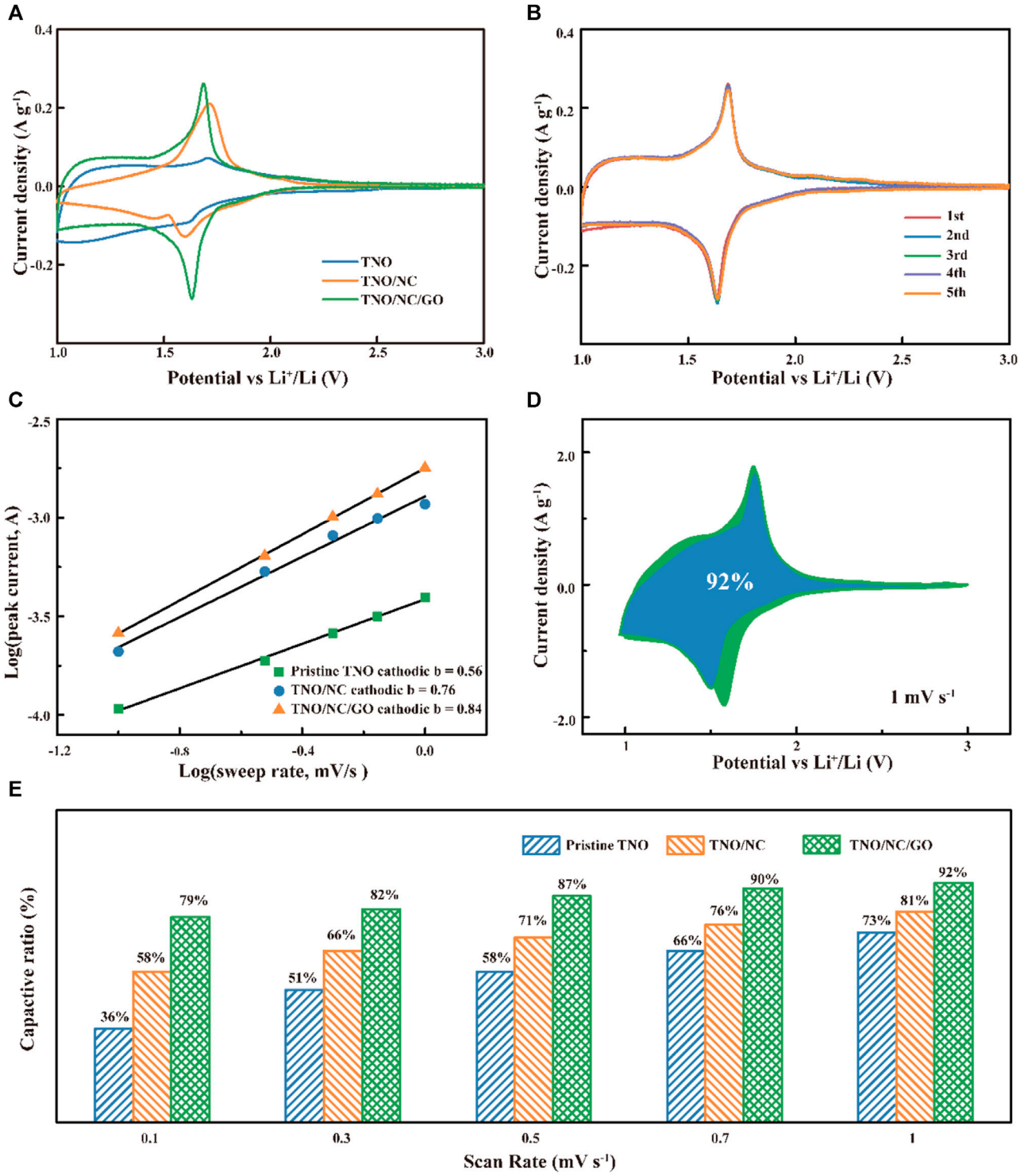

FIGURE 5 | (A) Comparison of cyclic voltammetry curves at a scan rate of 0.1 mV s^{-1}; **(B)** CV of TNO/NC/GO electrodes for LIBs. **(C)** the b-value obtained from the relationship between the peak current and sweep rate; **(D)** CV curves of TNO/NC/ GO with separation between total current and capacitive currents at 1 mV s^{-1}; **(E)** capacitive contributions at different sweep rates for different samples.

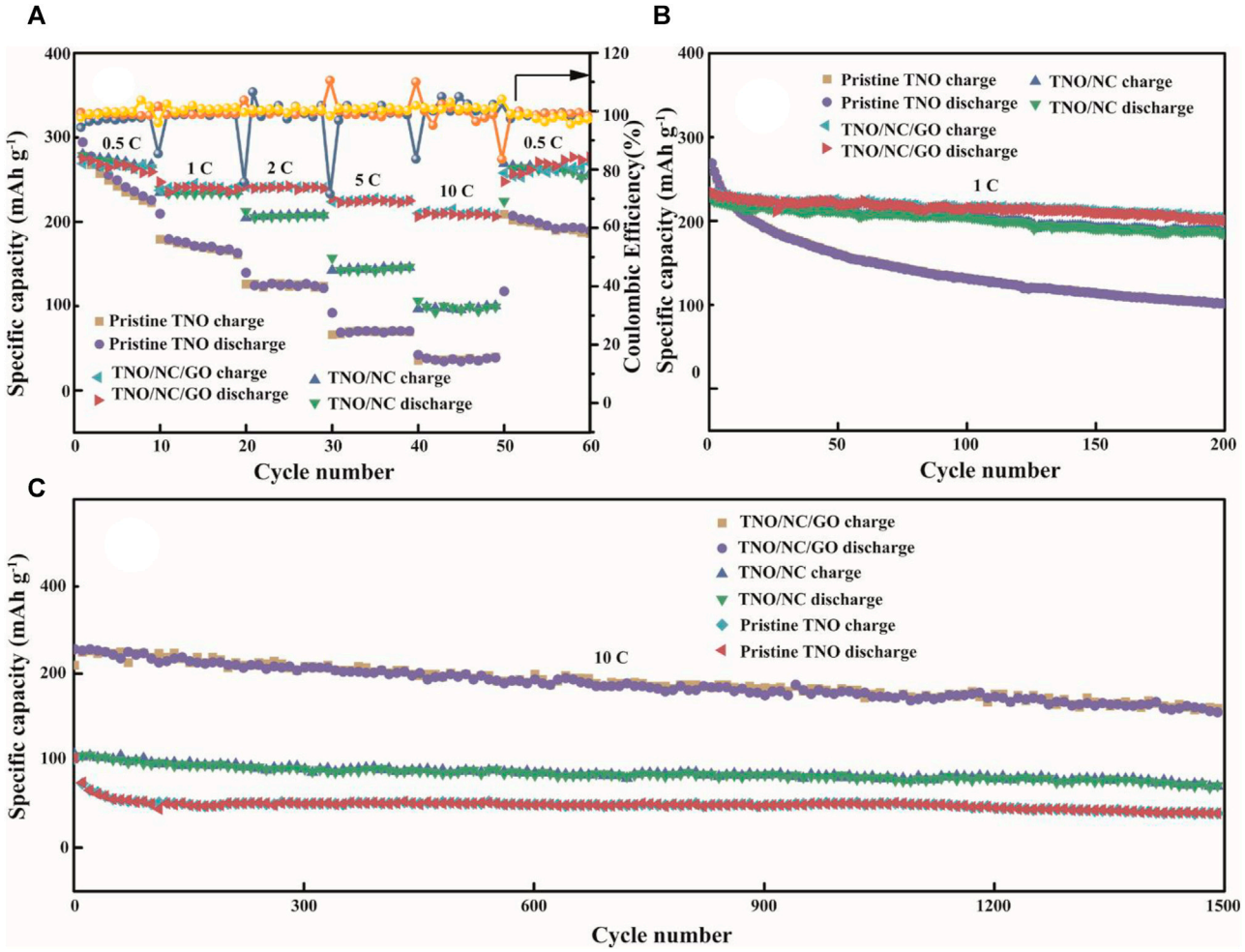

FIGURE 6 | (A) Rate capabilities of pristine TNO, TNO/NC, and TNO/NC/GO at various rates; cycling stability **(B)** at 1C and **(C)** at 10C.

mostly by the pseudocapacitive Li^+ charge storage. It is evident that the contribution of pseudocapacitive storage in TNO/NC/GO is superior to that of pristine TNO and TNO/NC across the entire potential range.

To quantitatively separate the contribution of diffusion-controlled and surface capacitive-controlled elements, the relationship between the current response and scan rate can be described by the following equation (Han et al., 2019):

$$i(V) = k_1 v + k_2 v^{1/2} \quad (8)$$

Figure 5D demonstrates the contributions from diffusion-controlled (black-brown region) and the surface capacitive-controlled (green region) storage mechanisms for TNO/NC/GO composites. Specifically, the surface capacitive-controlled contribution to the overall charge stored is calculated by the green enclosed area, demonstrating a significant percentage of 92% at a relatively high scan rate of 1.0 mV s^{-1}. Similarly, we also analyzed the contribution percentages of capacities of pristine TNO and TNO/NC electrode based on various scan rates in **Figure 5E**. Obviously, a larger portion of pseudocapacitive region in TNO/NC/GO than that of pristine TNO and TNO/NC can be clearly observed, exhibits better pseudocapacitive behaviors than pristine TNO and TNO/NC. As the scan rate gradually increases, the proportion of pseudocapacitive region becomes larger. According to previous reports, the graphene wrapped nanostructures enhance their pseudocapacitive behavior that promotes reversible electrochemical reaction. Therefore, by introducing interconnected porous graphene structure, pseudocapacitive contribution can be greatly enhanced, generating the high-rate capability and outstanding cycle stability of TNO/NC/GO.

In order to study the fast kinetics of lithium-ion transport, the rate performances were executed at 0.5–10 C within 1–3 V. **Supplementary Figure S3D** presents the galvanostatic discharge and charge curves of the TNO/NC/GO as anodes at different current densities. During the discharge process at 0.5°C, the voltage plateau is located at 1.60 V, while upon charge process, the plateau is observed at 1.7 V. These voltage plateaus are consistent with the aforementioned results of

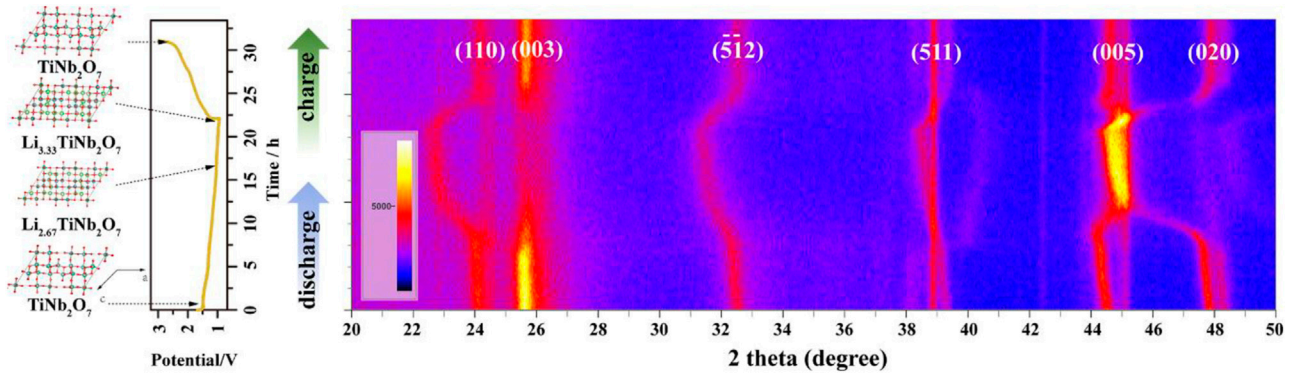

FIGURE 7 | *In situ* XRD patterns of TNO/NC/GO in the 2θ range of 20–50°.

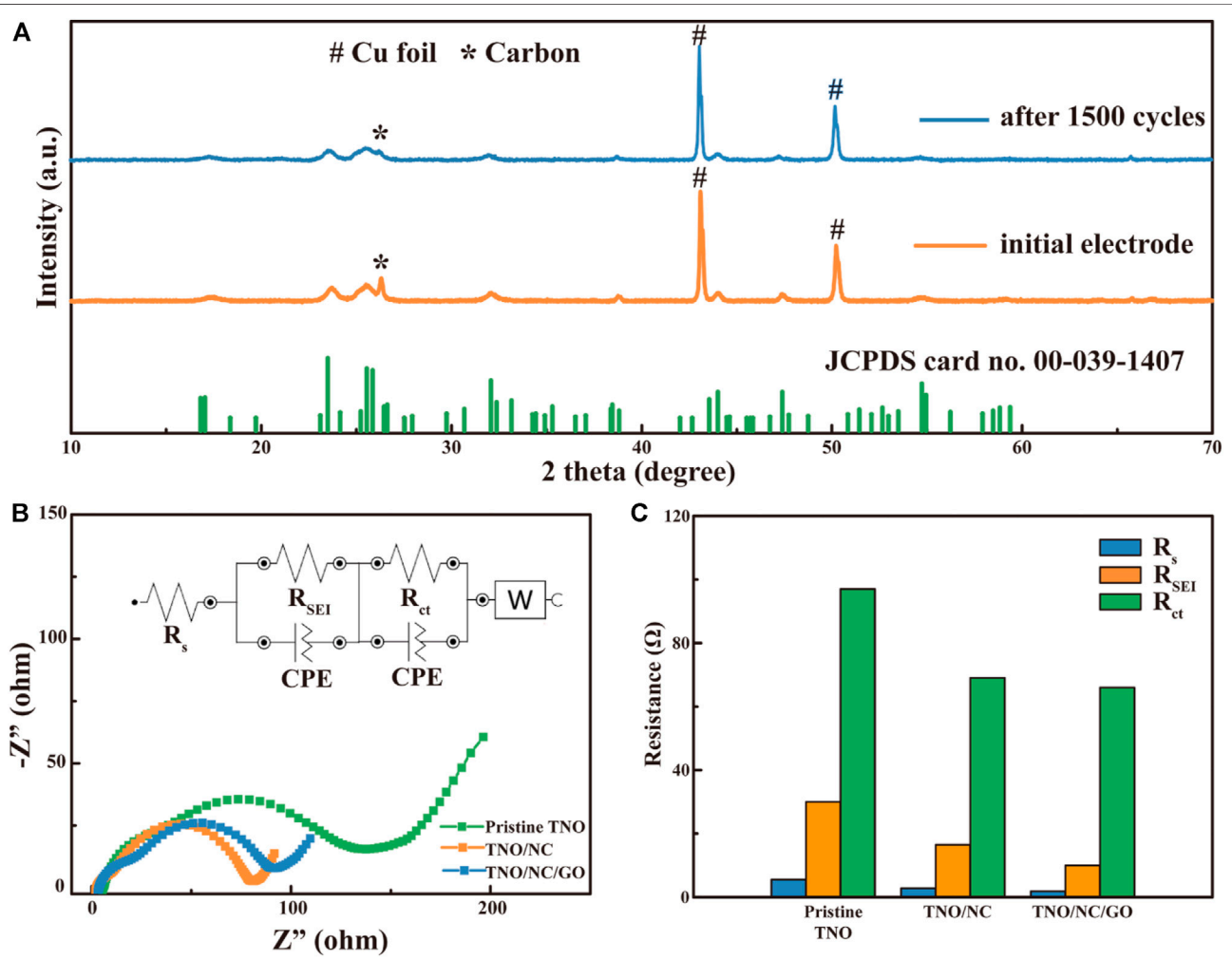

FIGURE 8 | (A) The XRD patterns of as-prepared and cycled TNO/NC/GO electrode a, **(B)** Nyquist plots of pristine TNO, TNO/NC, and TNO/NC/GO cells; the inset exhibits the selected equivalent circuit to fit the plots; **(C)** contribution of resistence of TNO, TNO/NC, and TNO/NC/GO electrode.

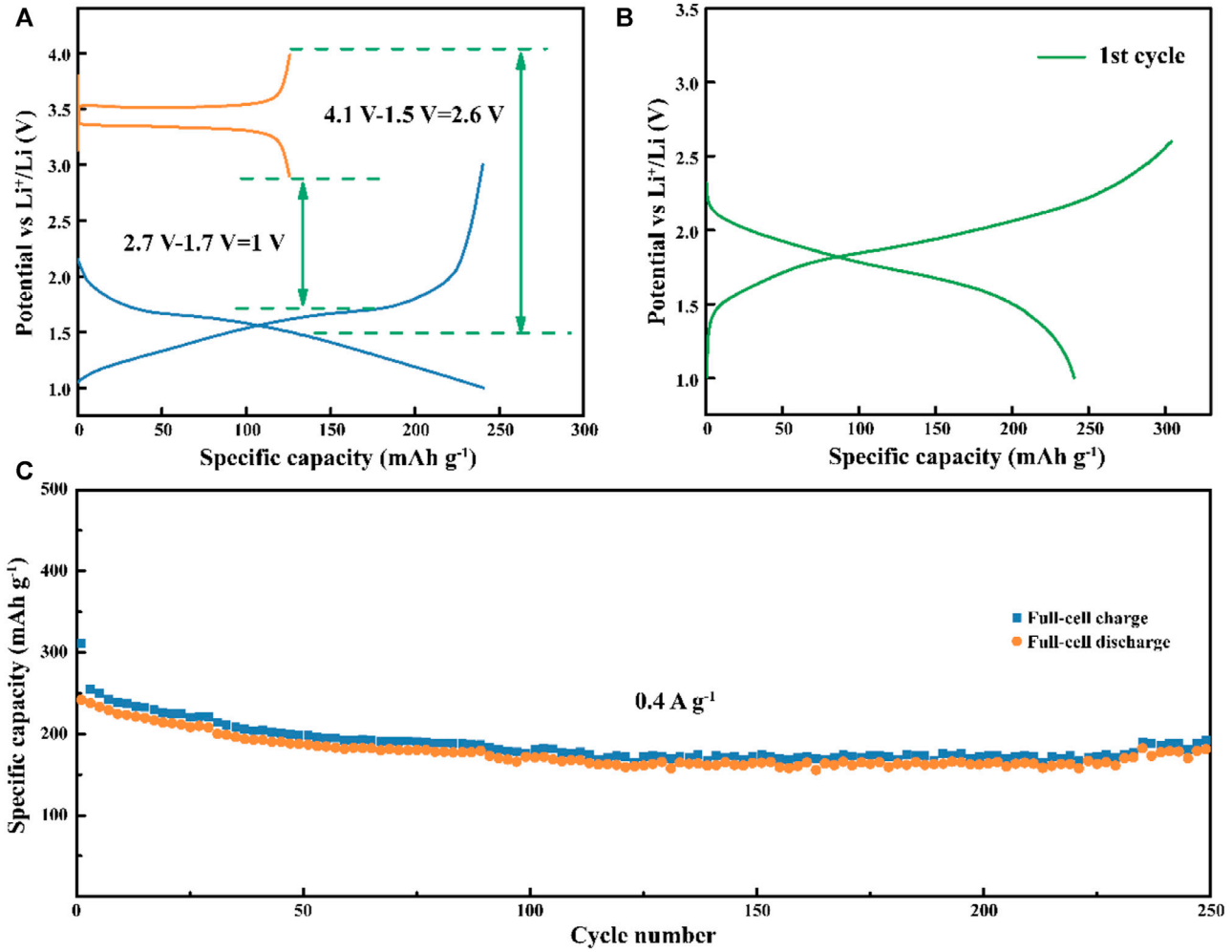

FIGURE 9 | (A) Details of capacity match up in $LiFePO_4$//$TiNb_2O_7$ full cell; **(B)** voltage profiles of $LiFePO_4$//$TiNb_2O_7$ full cell; **(C)** cyclic performance of $LiFePO_4$// $TiNb_2O_7$ full cell.

CVs. As the current rate raised from 0.5 to 10°C rate (**Figure 6A**), the average discharge capacity of TNO/NC/GO decreased from 264.2, 239.1, 238.8, 222.1, and 212.4 mA h g^{-1} at a charge/discharge rate of 1, 2, 5, and 10°C, respectively. As the current rate returns back to 0.5°C, the capacity also recovers back to 267.9 mA h g^{-1}, indicating good electrochemical reversibility of the TNO/NC/GO electrode. The cycling performance of the three samples at 1°C is presented in **Figure 6B**. the TNO/NC/GO electrode presents much more outstanding than the other two samples. After 200 cycles the capacity of the TNO/NC/GO electrode reaches 201.1 mA h g^{-1}, corresponding to a capacity retention ratio of 85%, while just 102.1 $mAhg^{-1}$ remained of the pristine TNO. At the same time, it is worth noting that long cycling performance is also a critical parameter for fast charging material. The long-term cycling ability of TNO/NC/GO electrodes at a charge/discharge rate of 10 C was achieved in **Figure 6C**, the capacity of the first and 1500th cycle is 217 and 166 mA h g^{-1}, respectively, reflecting a capacity retention of 76%. The Coulombic efficiency was found to be nearly 100% in each cycle. The results also manifest that TNO/NC/GO compound is a promising anode material owing to the excellent structural integrity and crystallinity.

To trace the real-time structural changes and electrochemical mechanism for TNO/NC/GO during the discharging and charging process, an *in situ* XRD experiment is performed at a low current rate of 0.1 C. As shown in **Figure 7**, the angle range is chosen from 20 to 50°, the purpose is to better and more clearly reflect the structural evolutions of the $TiNb_2O_7$ electrode. The initial lattice parameters a, b, and c are 20.3435 Å, 3.8000 Å, and 11.7948 Å, respectively. Besides, the initial lattice volume for TNO/NC/GO is 790.2 $Å^3$. During the discharging process, the (110) peak located at 23.9° obviously moves to a lower angle shifts due to Li^+ intercalation, indicating the gradual conversion from $TiNb_2O_7$ to $Li_{2.67}TiNb_2O_7$ (Catti et al., 2015). From the high-resolution images (**Figure 4D**), the exposed facet is (110), which undoubtedly provides convenience for lithium ion intercalation. Subsequently, only diffraction peaks belonging to $Li_{3.33}TiNb_2O_7$ appeared at the end of the discharge process (Catti et al., 2015). The calculated lattice volume of discharge products was

861.4 Å^3, which indicates volume expansion of 8.9% after full lithiation. This result is consistent with previous reports obtained by Guo et al. (2014) (7.22%) and (8.5%) Ise et al. (2018), much smaller than that for Si anode (300%). Therefore, the smaller volume expansion is also the main reason for the excellent performance of TNO electrode material, which has demonstrated superior electrochemical performance without degradation after 1500 cycles.

To verify the structural stability of the as-prepared sample, XRD pattern of cycled TNO/NC/GO in comparison with as-prepared electrode before assembling into batteries was also shown in **Figure 8A**, the XRD characteristic peaks of cycled TNO/NC/GO is similar to that of the as-prepared electrode, giving one hint that the TNO/NC/GO is stable enough after cycles at a current density of 10°C. To further investigate the beneficial effects of carbon coating, the EIS spectra of pristine TNO, TNO/NC, and TNO/NC/GO cells were collected, their corresponding Nyquist plots are revealed in **Figure 8B**. Typically, the Nyquist plot is normally composed of two depressed semicircles and an inclined. A semicircle in the high-frequency (HF) region is regarded as solid film resistance and the semicircle in the middle-frequency (MF) range is related to the charge-transfer resistance (Noh and Choi, 2016). The Nyquist plots were fitted by employing the equivalent circuit model shown in the inset of **Figure 8B**. According to the fitting results, the terms Rs respectively correspond to the resistance of the electrolyte, R_{SEI} interpreted as an interphase contact resistance. R_{ct} is the charge transfer resistance and its related capacitance. Moreover, the fitted results are also shown in **Figure 8C**. For these samples, the R_s values are similar, demonstrating that these electrodes in the fresh state exhibit similar electrolyte resistance. Compared to these samples, pristine TNO has a larger interphase contact resistance. In the meantime, TNO/NC/GO possess an obviously lower surface charge transfer (97 Ω) resistance compared to pristine TNO (66 Ω) and TNO/NC (69 Ω), indicating a much faster mass transport due to the effect of carbon coating.

To prove the feasibility of the TNO/NC/GO composite for practical energy storage applications, coin-type full cells were assembled using TNO/NC/GO composite as an anode and commercial $LiFePO_4$ as a cathode. The specific capacities of the anode and cathode at 0.4 A g^{-1} were separately estimated to be ~125 and 240 mAhg^{-1}, respectively (**Figure 9A**). According to the voltage range and specific capacities, the specific mass of electrode can be calculated over the voltage range from 1.0 to 2.6 V. The discharge/charge curves of the full-cell are displayed in **Figure 9B**. It had a reversible capacity of 182.7 mAhg^{-1} after 250 cycles (**Figure 9C**), corresponding to an energy density of 104 W h kg^{-1} (QV = 58.9 mA h g^{-1} × 1.78 V = 104 W h kg^{-1}, based on overall mass of anode and cathode). Overall, TNO/NC/GO composite can be a new promising material for the next-generation of practical energy storage devices as compared to some materials from previous studies.

CONCLUSION

In summary, a novel hierarchical TNO nanostructure was prepared successfully via an esterification reaction. The electronic conductivity was improved by forming a 3D wrapped carbon layer that was constructed via a simple cross-linked reaction by using PAM as flocculant. The fabricated TNO/NC/GO composite with stable framework exhibits superior storage performance to that of pristine TNO under identical conditions. It exhibits a high specific capacity of 264.2 mA h g^{-1} and excellent cyclability with extremely less capacity loss after 1500 cycles. This method opens up a novel method for the fabrication of hierarchical TNO nanoarchitectures materials. Moreover, our carbon coating strategy will fasten the commercialization of TNO materials in the next generation of lithium ion batteries.

DATA AVAILABILITY STATEMENT

The original contributions presented in the study are included in the article/**Supplementary Material**. Further inquiries can be directed to the corresponding authors.

AUTHOR CONTRIBUTIONS

Experimental, LH. YC. and LW. data analysis, L.H. J.L. and Y.T; writing—original draft preparation, L.H. writing—original and editing, H.Z. supervision, HZ and XY. All authors have read and agreed to the submitted.

FUNDING

This work was financially supported by the National Key Research and Development Program of China (No. 2019YFA0705601), the National Natural Science Foundation of China (No. 21878308), the Key Science and Technology Special Project of Henan Province (No. 202102210106), Zhengzhou Major Science and Technology Projects (No. 2019CXZX0074), the Key Program of Chinese Academy of Sciences (ZDRW_CN_2020–1).

SUPPLEMENTARY MATERIAL

The Supplementary Material for this article can be found online at: https://www.frontiersin.org/articles/10.3389/fenrg.2021.794527/full#supplementary-material

REFERENCES

Ashish, A. G., Arunkumar, P., Babu, B., Manikandan, P., Sarang, S., and Shaijumon, M. M. (2015). TiNb2O7/Graphene Hybrid Material as High Performance Anode for Lithium-Ion Batteries. *Electrochimica Acta* 176, 285–292. doi:10.1016/j.electacta.2015.06.122

Baek, S. W., Wyckoff, K. E., Butts, D. M., Bienz, J., Likitchatchawankun, A., Preefer, M. B., et al. (2021). Operando Calorimetry Informs the Origin of Rapid Rate Performance in Microwave-Prepared TiNb2O7 Electrodes. *J. Power Sourc.* 490, 229537. doi:10.1016/j.jpowsour.2021.229537

Catti, M., Pinus, I., and Knight, K. (2015). Lithium Insertion Properties of Li TiNb2O7 Investigated by Neutron Diffraction and First-Principles Modelling. *J. Solid State. Chem.* 229, 19–25. doi:10.1016/j.jssc.2015.05.011

Chen, C., Huang, Y., Zhang, H., Wang, X., Li, G., Wang, Y., et al. (2015). Small Amount of Reduce Graphene Oxide Modified Li4Ti5O12 Nanoparticles for Ultrafast High-Power Lithium Ion Battery. *J. Power Sourc.* 278, 693–702. doi:10.1016/j.jpowsour.2014.12.075

Ding, S., Wang, Y., Hong, Z., Lü, X., Wan, D., and Huang, F. (2011). Biomolecule-assisted Route to Prepare Titania Mesoporous Hollow Structures. *Chem. Eur. J.* 17 (41), 11535–11541. doi:10.1002/chem.201101314

Fu, X., Wang, B., Chen, C., Ren, Z., Fan, C., and Wang, Z. (2014). Controllable Synthesis of Spherical Anatase Mesocrystals for Lithium Ion Batteries. *New J. Chem.* 38 (10), 4754–4759. doi:10.1039/c4nj00543k

Gao, J., Cheng, X., Lou, S., Ma, Y., Zuo, P., Du, C., et al. (2017). Self-doping Ti1-Nb2+O7 Anode Material for Lithium-Ion Battery and its Electrochemical Performance. *J. Alloys Comp.* 728, 534–540. doi:10.1016/j.jallcom.2017.09.045

Guo, B., Yu, X., Sun, X.-G., Chi, M., Qiao, Z.-A., Liu, J., et al. (2014). A Long-Life Lithium-Ion Battery with a Highly Porous TiNb2O7 Anode for Large-Scale Electrical Energy Storage. *Energy Environ. Sci.* 7 (7), 2220–2226. doi:10.1039/c4ee00508b

Guo, Q., Zeng, W., Liu, S.-L., Li, Y.-Q., Xu, J.-Y., Wang, J.-X., et al. (2021). Recent Developments on Anode Materials for Magnesium-Ion Batteries: a Review. *Rare Met.* 40 (2), 290–308. doi:10.1007/s12598-020-01493-3

Han, C., He, Y.-B., Li, B., Li, H., Ma, J., Du, H., et al. (2014). Highly Crystalline Lithium Titanium Oxide Sheets Coated with Nitrogen-Doped Carbon Enable High-Rate Lithium-Ion Batteries. *ChemSusChem* 7 (9), 2567–2574. doi:10.1002/cssc.201402305

Han, J.-T., Huang, Y.-H., and Goodenough, J. B. (2011). New Anode Framework for Rechargeable Lithium Batteries. *Chem. Mater.* 23 (8), 2027–2029. doi:10.1021/cm200441h

Han, Y., Li, T., Li, Y., Tian, J., Yi, Z., Lin, N., et al. (2019). Stabilizing Antimony Nanocrystals within Ultrathin Carbon Nanosheets for High-Performance K-Ion Storage. *Energ. Storage Mater.* 20, 46–54. doi:10.1016/j.ensm.2018.11.004

He, S.-R., Zou, J.-P., Chen, L.-B., and Chen, Y.-J. (2021). A Nanostructured Ni/T-Nb2O5@carbon Nanofibers as a Long-Life Anode Material for Lithium-Ion Batteries. *Rare Met.* 40 (2), 374–382. doi:10.1007/s12598-020-01444-y

Hu, L., Meng, X., Liu, L., Liang, D., Liang, S., Wang, L.-L., et al. (2021). A Superficial Sulfur Interfacial Control Strategy for the Fabrication of a Sulfur/Carbon Composite for Potassium–Sulfur Batteries[J]. *Chem. Commun.* 57 (12), 1490–1493. doi:10.1039/D0CC07166H

Hummers, W. S., and Offeman, R. E. (1958). Preparation of Graphitic Oxide. *J. Am. Chem. Soc.* 80 (6), 1339. doi:10.1021/ja01539a017

Ise, K., Morimoto, S., Harada, Y., and Takami, N. (2018). Large Lithium Storage in Highly Crystalline TiNb2O7 Nanoparticles Synthesized by a Hydrothermal Method as Anodes for Lithium-Ion Batteries. *Solid State Ionics* 320, 7–15. doi:10.1016/j.ssi.2018.02.027

Kankanige, D., and Babel, S. (2021). Contamination by ≥6.5 μm-sized Microplastics and Their Removability in a Conventional Water Treatment Plant (WTP) in Thailand. *J. Water Process Eng.* 40, 101765. doi:10.1016/j.jwpe.2020.101765

Kumar, A., and Sahay, P. P. (2019). Microstructural, Optical and Electrochromical Properties of W-Doped Nb2O5 Thin Films Prepared by Dip-Coating Process Using Sols Obtained by the Chloroalkoxide Route. *J. Mater. Sci. Mater. Electron.* 30 (19), 17999–18014. doi:10.1007/s10854-019-02153-8

Li, S., Cao, X., Schmidt, C. N., Xu, Q., Uchaker, E., Pei, Y., et al. (2016). TiNb2O7/graphene Composites as High-Rate Anode Materials for Lithium/sodium Ion Batteries. *J. Mater. Chem. A.* 4 (11), 4242–4251. doi:10.1039/c5ta10510b

Lin, C., Hu, L., Cheng, C., Sun, K., Guo, X., Shao, Q., et al. (2018). Nano-TiNb2O7/carbon Nanotubes Composite Anode for Enhanced Lithium-Ion Storage. *Electrochimica Acta* 260, 65–72. doi:10.1016/j.electacta.2017.11.051

Lin, C., Yu, S., Wu, S., Lin, S., Zhu, Z.-Z., Li, J., et al. (2015). Ru0.01Ti0.99Nb2O7 as an Intercalation-type Anode Material with a Large Capacity and High Rate Performance for Lithium-Ion Batteries. *J. Mater. Chem. A.* 3 (16), 8627–8635. doi:10.1039/c5ta01073j

Liu, A., Zhang, H., Xing, C., Wang, Y., Zhang, J., Zhang, X., et al. (2021). Intensified Energy Storage in High-Voltage Nanohybrid Supercapacitors via the Efficient Coupling between TiNb2O7/Holey-rGO Nanoarchitectures and Ionic Liquid-Based Electrolytes. *ACS Appl. Mater. Inter.* 13 (18), 21349–21361. doi:10.1021/acsami.1c03266

Liu, K., Wang, J.-a., Yang, J., Zhao, D., Chen, P., Man, J., et al. (2021). Interstitial and Substitutional V5+-Doped TiNb2O7 Microspheres: A Novel Doping Way to Achieve High-Performance Electrodes. *Chem. Eng. J.* 407, 127190. doi:10.1016/j.cej.2020.127190

Liu, M., Dong, H., Zhang, S., Chen, X., Sun, Y., Gao, S., et al. (2019). Three-dimensional Porous $TiNb_2O_7$/CNT-KB Composite Microspheres as Lithiumion Battery Anode Material. *ChemElectroChem* 6 (15), 3959–3965. doi:10.1002/celc.201901024

Lou, S., Cheng, X., Zhao, Y., Lushington, A., Gao, J., Li, Q., et al. (2017). Superior Performance of Ordered Macroporous TiNb 2 O 7 Anodes for Lithium Ion Batteries: Understanding from the Structural and Pseudocapacitive Insights on Achieving High Rate Capability. *Nano Energy* 34, 15–25. doi:10.1016/j.nanoen.2017.01.058

Lou, S., Ma, Y., Cheng, X., Gao, J., Gao, Y., Zuo, P., et al. (2015). Facile Synthesis of Nanostructured TiNb2O7 Anode Materials with superior Performance for High-Rate Lithium Ion Batteries. *Chem. Commun.* 51 (97), 17293–17296. doi:10.1039/c5cc07052j

Lu, X., Jian, Z., Fang, Z., Gu, L., Hu, Y.-S., Chen, W., et al. (2011). Atomic-scale Investigation on Lithium Storage Mechanism in TiNb2O7,. *Energ. Environ. Sci.* 4 (8), 2638–2644. doi:10.1039/c0ee00808g

Noh, H., and Choi, W. (2016). Preparation of a TiNb2O7Microsphere Using Formic Acid and Wrapping with Reduced Graphene Oxide for Anodes in Lithium Ion Batteries. *J. Electrochem. Soc.* 163 (6), A1042–A1049. doi:10.1149/2.1181606jes

Park, H., Song, T., and Paik, U. (2015). Porous TiNb2O7 Nanofibers Decorated with Conductive Ti1−xNbxN Bumps as a High Power Anode Material for Li-Ion Batteries. *J. Mater. Chem. A.* 3 (16), 8590–8596. doi:10.1039/c5ta00467e

Park, S.-K., Lee, J., Hwang, T., and Piao, Y. (2017). Sulfur-loaded Monodisperse Carbon Nanocapsules Anchored on Graphene Nanosheets as Cathodes for High Performance Lithium-Sulfur Batteries. *J. Mater. Chem. A.* 5 (3), 975–981. doi:10.1039/c6ta08557a

Tang, K., Mu, X., van Aken, P. A., Yu, Y., and Maier, J. (2013). "Nano-Pearl-String" TiNb2O7as Anodes for Rechargeable Lithium Batteries. *Adv. Energ. Mater.* 3 (1), 49–53. doi:10.1002/aenm.201200396

Thiyagarajan, G. B., Shanmugam, V., Wilhelm, M., Mathur, S., Moodakare, S. B., and Kumar, R. (2021). TiNb2O7-Keratin Derived Carbon Nanocomposites as Novel Anode Materials for High-Capacity Lithium-Ion Batteries. *Open Ceramics* 6, 100131. doi:10.1016/j.oceram.2021.100131

Yang, C., Deng, S., Lin, C., Lin, S., Chen, Y., Li, J., et al. (2016). Porous TiNb24O62microspheres as High-Performance Anode Materials for Lithium-Ion Batteries of Electric Vehicles. *Nanoscale* 8 (44), 18792–18799. doi:10.1039/c6nr04992c

Yang, R., Zhang, X.-J., Fan, T.-F., Jiang, D.-P., and Wang, Q. (2020). Improved Electrochemical Performance of Ternary Sn-Sb-Cu Nanospheres as Anode Materials for Lithium-Ion Batteries. *Rare Met.* 39 (10), 1159–1164. doi:10.1007/s12598-014-0303-6

Yang, Y., Li, Y., Liu, K., Zhang, K., Jin, S., Bao, Y., et al. (2021). Hierarchical Porous TiNb2O7@N-Doped Carbon Microspheres as superior Anode Materials for Lithium Ion Storage. *Int. J. Hydrogen Energ.* 46 (5), 3425–3436. doi:10.1016/j.ijhydene.2020.10.190

Yang, Y., Li, Z., Zhang, R., Ding, Y., Xie, H., Liu, G., et al. (2021). Polydopamine-derived N-Doped Carbon-Coated Porous TiNb2O7 Microspheres as Anode Materials with superior Rate Performance for Lithium-Ion Batteries. *Electrochimica Acta* 368, 137623. doi:10.1016/j.electacta.2020.137623

Yin, L., Pham-Cong, D., Jeon, I., Kim, J.-P., Cho, J., Jeong, S.-Y., et al. (2020). Electrochemical Performance of Vertically Grown WS_2 Layers on $TiNb_2O_7$

Nanostructures for Lithium-Ion Battery Anodes. *Chem. Eng. J.* 382, 122800. doi:10.1016/j.cej.2019.122800

Zhang, Z.-J., Li, W.-J., Chou, S.-L., Han, C., Liu, H.-K., and Dou, S.-X. (2021). Effects of Carbon on Electrochemical Performance of Red Phosphorus (P) and Carbon Composite as Anode for Sodium Ion Batteries. *J. Mater. Sci. Tech.* 68, 140–146. doi:10.1016/j.jmst.2020.08.034

Zhang, Z.-J., Zhao, J., Qiao, Z.-J., Wang, J.-M., Sun, S.-H., Fu, W.-X., et al. (2021). Nonsolvent-induced Phase Separation-Derived TiO2 Nanotube Arrays/porous Ti Electrode as High-Energy-Density Anode for Lithium-Ion Batteries. *Rare Met.* 40 (2), 393–399. doi:10.1007/s12598-020-01571-6

Zhu, G., Jiao, W., Li, Q., Zhao, Y., Liu, X., and Che, R. (2022). Conductivity Optimization via Intertwined CNTs between TiNb2O7@C Microspheres for a superior Performance Li-Ion Battery Anode. *J. Colloid Interf. Sci.* 607, 1103–1108. doi:10.1016/j.jcis.2021.09.003

Zhu, G., Li, Q., and Che, R. (2018). Hollow TiNb2 O7 @C Spheres with Superior Rate Capability and Excellent Cycle Performance as Anode Material for Lithium-Ion Batteries. *Chem. Eur. J.* 24 (49), 12932–12937. doi:10.1002/chem.201801728

Conflict of Interest: The authors declare that the research was conducted in the absence of any commercial or financial relationships that could be construed as a potential conflict of interest.

Publisher's Note: All claims expressed in this article are solely those of the authors and do not necessarily represent those of their affiliated organizations, or those of the publisher, the editors, and the reviewers. Any product that may be evaluated in this article, or claim that may be made by its manufacturer, is not guaranteed or endorsed by the publisher.